Statistical Analysis of Remote Precipitation in Japan Caused by Typhoons in September

Shinichi KODAMA[1]

Atmosphere and Ocean Research Institute
The University of Tokyo, Kashiwa, Japan

and

Masaki SATOH

Atmosphere and Ocean Research Institute
The University of Tokyo, Kashiwa, Japan

October 20, 2021

----

1) Corresponding author: Shinichi Kodama, Atmosphere and Ocean Research Institute The University of Tokyo, 5-1-5, Kashiwanoha, Kashiwa-shi, Chiba 277-8564 Japan.
Email: kodama@aori.u-tokyo.ac.jp

Abstract

During the autumn rainy season, typhoons located far from Japan sometimes cause significant precipitation in Japan. In this study, we characterized remote precipitation events in September for 40 years from 1980 to 2019. We also analyzed cases in which remote precipitation did not occur despite approaching typhoons, as well as cases in which heavy precipitation was not affected by typhoons. We characterized the environmental fields of the remote precipitation cases by comparing them with these other two cases.

Statistical analysis showed that remote precipitation tended to occur when the typhoons were located over the southern or southwestern oceans of mainland Japan and when the tracks of the typhoons were northward or recurving. The composite analysis of the remote precipitation cases showed that the extension of the subtropical high was retreating to the east for the two days before the remote precipitation. By contrast, the cases in which remote precipitation did not occur showed the opposite pattern: the extension of the subtropical high was strengthening to the west when typhoons were approaching over the southern or southwestern oceans of the Japanese archipelago. Furthermore, the remote precipitation occurred to the equatorward jet streak entrance of the 200 hPa jet, whereas the 200 hPa jet streak was shifted to the west in the cases where remote precipitation did not occur. The vertical cross-section of the northward water vapor flux showed that the northward water vapor inflow from the middle troposphere was larger in cases of remote precipitation than in cases in which heavy precipitation was not caused by typhoons. In addition, our results suggest that the contribution of the wind speed to this difference in the water vapor flux was greater than that of the water vapor mixing ratio.

Keywords typhoon; remote precipitation; water vapor flux; autumn rainy season

1. Introduction

During the autumn rainy (Akisame, in Japanese) season, typhoons located far from Japan can increase the supply of water vapor in Japan, resulting in significant precipitation. Wang et al. (2009) referred to this type of precipitation as remote precipitation due to the indirect effect of typhoons and distinguished it from precipitation due to the direct effect of typhoons, i.e., the effects of the eyewall and spiral rain bands. Remote precipitation is thought to be caused generally by warm and moist northward winds to the east of the typhoons, which stimulate the Akisame front.

There have been several studies on remote precipitation in Japan caused by the indirect effect of typhoons during the Akisame season. Wang et al. (2009) conducted the hypothetical typhoon vortex removal experiment for Typhoon Songda in 2004, which suggested the importance of the northward water vapor transport enhanced by the typhoon. Murata (2009) argued that in addition to the supply of water vapor, the dynamic effect of mountainous terrain contributed to the remote precipitation for Typhoon Meari in 2004. Ninomiya (2013) pointed out the influence of a weak shortwave mid-latitude trough on the remote precipitation caused by Typhoon TRIX in 1965. Moreover, Kitabatake (2002) suggested that the involvement of frontogenesis and associated vertical motion was responsible for the heavy remote precipitation caused by Typhoon Saomai in 2000. Saito (2019) and Saito and Matsunobu (2020) have described the influence of upper-level ageostrophic winds on the remote precipitation caused by Typhoon Melor in 2009.

Remote precipitation caused by typhoons is also observed in the Baiu season (early summer rainy season). Using potential vorticity analysis, Yoshida and Itoh (2012) revealed that the indirect supply of water vapor from Typhoon Maggie in 1999 caused remote precipitation. Hirata and Kawamura (2014) statistically analyzed the remote impact on Japan of two primary tracks of typhoons in the Baiu season. In addition, Kawamura and Ogasawara (2006) and Yamada and Kawamura (2007) studied the interaction between typhoons and the Pacific-Japan pattern from the Baiu season to the Akisame season and found that the remote precipitation is related to the strengthening of the subtropical high to the east of Japan.

Research on East Asian regions other than Japan has also been conducted. Byun and Lee (2012) performed a statistical analysis of remote precipitation cases on the Korean Peninsula, distinguishing between typhoons that made landfall in China and those that did not. Yuan et al. (2018) conducted a statistical analysis of the remote precipitation caused by tropical cyclones in the Bay of Bengal.

By contrast, a region of precipitation caused indirectly by the effects of tropical cyclones over North America is called a predecessor rain event (PRE) (Cote 2007). PRE is generally explained as a phenomenon in which tropical cyclones in the Atlantic Ocean recurve and move northward into the mid-latitudes, forming a rain band that stagnates on North America about 1000 km north of the tropical cyclones, resulting in heavy precipitation (Kitabatake 2012). Galarneau et al. (2010) conducted a statistical analysis of PRE in a 14-year period and analyzed in more detail the case of tropical cyclone Erin in 2007. Schumacher et al. (2011) studied the same tropical cyclone by conducting a sensitivity experiment with removal of water vapor. They showed that although the precipitation was enhanced by water vapor from Erin, it was the environmental field that generated the precipitation, even in the absence of Erin. Moreover, Schumacher et al. (2012) extracted both recurved and non-recurved conditions from the 2007 Erin and the 2008 Ike ensemble forecasts and found that the increased water vapor transport due to recurving did not necessarily enhance the precipitation. Many other studies have aimed to clarify the mechanism of PRE and the indirect effects of tropical cyclones (Bosart and Carr 1978; Ross and Kurihara 1995; Bosart et al. 2012; Moore et al. 2013).

The environmental fields of PRE in North America and of remote precipitation in Japan are very different, and their underlying mechanisms are not necessarily the same. PRE in North America occurs over land, while remote precipitation in Japan occurs mainly over the ocean or adjacent areas. However, they have some factors in common, such as the mid-latitude systems and water vapor transport from tropical cyclones. Despite many individual case studies, there have been no statistical analyses to clarify the mechanism of remote precipitation in Japan during the Akisame season. The purpose of this study is to identify the differences between the environmental fields of remote precipitation cases and those of cases in which remote precipitation did not occur even when typhoons were approaching. In addition, we compare remote precipitation cases with heavy precipitation cases that are not influenced by typhoons and clarify the effect of typhoons on remote precipitation from the viewpoint of water vapor flux.

2. Data and methods

2.1 Data

In this study, we used Best Track Data from the Regional Specialized Meteorological Center (RSMC) Tokyo-Typhoon Center, which provides information on typhoons occurring from 1951 to the present. For precipitation and other physical parameters, we used the European Centre for Medium-Range Weather Forecasts (ECMWF) Reanalysis v5 (ERA5) data, which provides a variety of physical parameters from 1950 to the present with a horizontal resolution of 0.25 degrees in latitude and longitude and 37 pressure levels from 1000 hPa to 1 hPa. Hourly data on pressure levels (Hersbach et al. 2018a), hourly data on single levels (Hersbach et al. 2018b) and monthly averaged data on single levels (Hersbach et al. 2019) were used in this study. The Global Satellite Mapping of Precipitation (GSMaP) (Kubota et al. 2007) was used to analyze the distribution and intensity of precipitation areas and to confirm the reproducibility of the ERA5 precipitation data. The GSMaP provides hourly data for rainfall intensity from 2000 to the present in the region 60°S–60°N with a horizontal resolution of 0.1 degrees in latitude and longitude.

2.2 Methods

The analysis period of this study is every September from 1980 to 2019. We first extracted the days when daily precipitation of 40 mm or more was recorded at 33 or more grid points in the rectangular domain covering the major part of Japan [130–150°E, 30–40°N], regardless of whether or not typhoons were approaching. The daily precipitation was obtained by totaling the hourly precipitation from 00 UTC to 23 UTC from the ERA5 data. The threshold value of 40 mm was selected to ensure that representative remote precipitation cases were included. The minimum number of 33 grid points was chosen because this represents about 1% of all grid points in the rectangular domain and excludes rainfall events that are too localized. The rectangular domain was chosen because it includes the area with mean September precipitation of about 250 mm or more, calculated from the 40 years of ERA5 data covering our study period. As a result, we obtained 618 precipitation days. Up to this point, we had not considered whether or not the precipitation was due to the indirect effects of typhoons.

To define the days when typhoons were remotely located, we referred to Tsuguti and Kato (2014); we extracted the cases in which the distance between a typhoon center and a precipitation center was between 500 km and 1500 km. Typhoons in this study are those with a maximum wind speed of at least 34 knots. Typhoons above 34 knots are classified as grades 3, 4, and 5 in the Best Track Data. The typhoon center was defined as the position at 12 UTC on the day of precipitation, and the precipitation center was defined as the location of maximum daily precipitation in the rectangular domain. In the case of multiple typhoons within 500–1500 km of the precipitation center on the same day, only the typhoon closest to the precipitation center was considered. In addition, to confirm the remote impact of typhoons on precipitation areas, we referred to Galarneau et al. (2010) to check the connection between the typhoon and the precipitation; we defined the precipitation as remote if both the typhoon center and the precipitation center were surrounded by a contour with daily average precipitable water of 50 mm or more. For cases of remote precipitation caused by the same typhoon, we counted only the first day on which the above criteria were satisfied. As a result, we extracted 58 remote precipitation cases. Hereafter, we refer to these cases of remote precipitation in Japan as “PRE” cases, to acknowledge their similarity to PRE in North America.

We also extracted the cases in which PRE did not occur, i.e., heavy precipitation did not occur even though typhoons were approaching Japan. These cases are hereafter referred to as “non-PRE” cases. To obtain these cases, we first extracted the days when daily precipitation of less than 40 mm was recorded at all grid points in the rectangular domain. From this list, we selected the cases in which the distance between the typhoon center and the median precipitation point, which was defined from the precipitation centers of the 58 PRE cases, was between 500 km and 1500 km. In addition, we excluded cases where the typhoons were determined to be typhoons of the extracted PRE cases. As with the PRE cases, for non-PRE cases caused by the same typhoon, we counted only the first day on which the above criteria were satisfied. As a result, 31 non-PRE cases were extracted.

Finally, we also extracted cases of heavy precipitation that was not due to the influence of typhoons. We defined the days when daily precipitation of 80 mm or more was recorded at 33 or more grid points in the rectangular domain. Next, we selected the cases in which the distance between the typhoon center and the precipitation center was more than 2000 km, as well as cases for which typhoons were not observed on the Best Track Data. Precipitation cases due to tropical depression (maximum wind speed of less than 34 knots, grade 2 on the Best Track Data) or extratropical cyclone (grade 6 on the Best Track Data) were also excluded. For cases of heavy precipitation on consecutive days, we counted only the first day. As a result, 24 cases of heavy precipitation without the influence of typhoons were extracted. These cases are hereafter referred to as "non-typhoon" cases.

3. Results

3.1 Statistical data

Figure 1 shows the positions of typhoon centers and precipitation centers for PRE, non-PRE, and non-typhoon cases, as well as the rectangular domain used to define the precipitation location. Statistical analysis of the PRE cases showed that the typhoon centers at the time of PRE occurrence were widely distributed in the zonal areas over the southern and southwestern oceans of Japan between 120°E and 150°E (Fig. 1a). The precipitation centers were also widely distributed within the rectangular domain [130–150°E, 30–40°N] (Fig. 1b). Most of the tracks of the typhoons were northward or recurving, with few westward typhoon tracks (Figs. 2a–2d). The distances between the typhoon center and the precipitation center were between 500 km and 1500 km, but distances of more than 1000 km were more frequent (Fig. 3a). Examination of the direction of the precipitation centers from the typhoon centers indicated that PRE tended to occur to the north to northeast of the typhoons (Fig. 3b). In other words, PRE tended to occur when the typhoons were located over the southern or southwestern oceans of the Japanese archipelago. Four cases were excluded from Fig. 3b because their azimuths were not within 90 degrees. Examination of the central pressure of the typhoons at the time of PRE occurrence showed that typhoons above 980 hPa, which were relatively weak, still caused PRE (Fig. 3c). For the typhoons that persisted for more than 6 days, we compared the time of minimum central pressure with the time of central pressure at PRE occurrence. We found that six typhoons occurred before the time of minimum central pressure, five typhoons occurred at the time of minimum central pressure, and 18 typhoons occurred after the time of minimum central pressure. This result is similar to that of the statistical analysis of North American PRE (Galarneau et al. 2010), in which tropical cyclones tended to weaken when PRE occurred. Finally, Figure 4 shows the relationship between the central pressure of the typhoons and the maximum daily precipitation. One case with extremely high precipitation was excluded. Figure 4 indicates that the intensity of the remote precipitation is not affected by the intensity of typhoons. Based on this result, we did not take into consideration the effects of the difference in the strength of typhoons on precipitation in the following analysis. The mean of the maximum daily precipitation of the 58 PRE cases was about 125 mm.

For the non-PRE cases, the typhoon centers were widely distributed, similar to those of the PRE cases (Fig. 1c vs 1a), but the typhoons tended to be located more eastward than those of the PRE cases. Most of the tracks of the typhoons were northward or recurving, but some typhoons moved westward without recurving (Figs. 2e–2h). We note that the typhoons with a relatively strong central pressure below 960 hPa did not cause remote precipitation in Japan, and were categorized as non-PRE typhoons (Fig. 3d).

The distribution of the precipitation centers of the 24 non-typhoon cases is shown in Fig. 1d. It is not so different from that of the PRE cases (Fig. 1b). The mean daily maximum precipitation of the extracted cases was about 157 mm.

3.2 Composite analysis

1) PRE cases

Time evolution of the horizontal distribution of the 500 hPa geopotential height (contour), the precipitable water (shaded), and the vertical integrals of water vapor flux (vector) were investigated by composite analysis (Fig. 5). These are the composite maps during the period from Day–2 (two days before PRE occurrence) to Day+1 (one day after PRE occurrence). In these composite analyses, we referred to Galarneau et al. (2010); the precipitation centers of the 58 PRE cases were shifted to their median values at Day0. The composite maps for Day–2, Day–1, and Day+1 were obtained after shifting the latitude and longitude by the same amount as at Day0 in each case. The results show that the high precipitable water exceeding 50 mm entered the rectangular domain from Day–2 to Day0, and the extension of the subtropical high (represented by the 5880 m line) was retreating to the east from Day–2 to Day0. The retreat of the subtropical high is similar to the OT cases (tropical cyclones over the East China Sea) on the Korean Peninsula (Byun and Lee 2012). Moreover, the clear northward water vapor flux was observed between the typhoons and the subtropical high on Day0 and Day+1. Figure 6 shows the composite maps of the 200 hPa geopotential height (black contour), the 200 hPa isotach (blue contour), the 700 hPa vertical velocity (shaded), and the 850 hPa horizontal wind (vector) from Day–2 to Day+1. The precipitation area (represented by the median point of precipitation and the 700 hPa ascending basin) was located on the equatorward jet streak entrance of the 200 hPa jet on Day0. This positional relationship is consistent with the PRE statistical analyses for North America and East Asia (Galarneau et al. 2010; Byun and Lee 2012; Moore et al. 2013; Yuan et al. 2018). In the lower troposphere at 850 hPa, northward horizontal winds were also observed at Day0 and Day+1. The 850 hPa equivalent potential temperature gradient at Day0 is relatively large over Japan, indicating a frontal structure (Fig. 7a). To identify the layer in which water vapor entered the precipitation areas, we show the vertical cross-section between 130°E and 150°E along the latitude 30°N, which corresponds to the lower edge of the rectangular domain (Fig. 7b). This shows that the water vapor flux entered up to the middle troposphere at 500 hPa. The details of the water vapor flux are discussed below.

2) Non-PRE cases

We constructed composite maps for the 16 non-PRE cases in which the typhoon centers were located within [130–140°E, 20–30°N] on Day0. The area was chosen because the typhoon centers were clustered there. Figure 8 shows the 500 hPa geopotential height (contour), the precipitable water (shaded), and the vertical integrals of water vapor flux (vector) from Day–2 to Day+1. In contrast to the PRE cases (Fig. 5), the high precipitable water exceeding 50 mm did not enter the rectangular domain from Day–2 to Day-0. In addition, the extension of the subtropical high was strengthening to the west from Day–2 to Day0; this was in contrast to the PRE cases, where the subtropical high was retreating. Moreover, the clear northward water vapor flux was not observed from Day–2 to Day0. Figure 9 shows the 200 hPa geopotential height (black contour), the 200 hPa isotach (blue contour), the 700 hPa vertical velocity (shaded), and the 850 hPa horizontal wind (vector) for 16 non-PRE cases from Day–2 to Day+1. This shows that the jet streak entrance was located more westward in the non-PRE cases than in the PRE cases. A similar result was obtained from previous East Asian PRE analysis (Yuan et al. 2018). The 850 hPa northward horizontal winds were not observed from Day–2 to Day0. In addition, the 850 hPa equivalent potential temperature for the non-PRE cases on Day0 had a weaker gradient than in the PRE cases, indicating that the front over Japan was more obscure than in the PRE cases (Fig. 10). The northward water vapor flux component was hardly seen compared to that of the PRE cases (not shown).

3) Non-typhoon cases

In the non-typhoon cases, as in the PRE cases, we made composite maps by aligning the precipitation centers of the 24 cases to the point of their median value. On Day0, the subtropical high extended far to the west, and the precipitation area was located on the equatorward jet streak entrance of the 200 hPa jet (Figs. 11a, b). The 850 hPa equivalent potential temperature on Day0 indicates that a frontal zone locates over mainland Japan, as in the PRE cases (Fig. 11c). Although the northward water vapor flux component was observed in the lower troposphere at around 900 hPa, it was not clearly seen in the middle troposphere (Fig. 11d). The northward water vapor flux was smaller than that in the PRE cases (Fig. 7b).

4. Discussion

The composite analysis of the PRE cases showed that the extension of the subtropical high was retreating to the east from Day–2 to Day0, while the non-PRE cases showed it strengthening to the west; the tendencies of the extension of the subtropical high are opposite for the PRE cases and the non-PRE cases. Because the typhoons on Day0 in the non-PRE cases were located more eastward than in the PRE cases (Fig. 1), we compared the tendencies of the extension of the subtropical high using the cases in which the typhoons are located in about the same area. Composite maps were created for 16 non-PRE cases in which the typhoon centers on Day0 were located within the area [130–140°E, 20–30°N]. Then, we analyzed 18 PRE cases in which the typhoon centers were located within the same area. The time series of the composite of 500 hPa geopotential height averaged over the region [130–140°E, 27.5–32.5°N] is shown in Fig. 12, which shows the change in the geopotential height from 48 hours before PRE occurrence. The region [130–140°E, 27.5–32.5°N] was chosen because water vapor was particularly entering the precipitation area from that region. The periodic variations for both the PRE and non-PRE cases represent the daily variation in the subtropical high. The change in the geopotential height from Day–2 (–48 h) to Day0 shows a decreasing tendency in the PRE cases and an increasing tendency in the non-PRE cases, confirming the characteristic differences in the extension of the subtropical high between the two groups.

In the non-PRE cases, the area of the jet streak entrance was located more to the west than in the PRE cases, and there was no clear frontal area over Japan. Mid-latitude factors such as a jet streak and a front are important in determining whether remote precipitation will eventually occur. However, the extension of the subtropical high, which influences the amount of northward water vapor transport, may also be important in determining whether or not PRE occurs when typhoons are approaching. To clarify the mechanism of the extending change of the subtropical high during approaching typhoons, it is necessary to understand the dynamics of the interaction between typhoons and the subtropical high.

Vertical cross-sections of the northward water vapor flux component for the PRE cases and the non-typhoon cases showed that water vapor flux was observed mainly in the lower troposphere in both cases, but differed between the two cases in the middle troposphere (Figs. 7b, 11d). We analyzed this difference in the northward water vapor flux component further. The water vapor flux is a product of air density ρ, water vapor mixing ratio q_v, and wind speed v. We investigated whether q_v or v contributed more to the difference in the water vapor flux by ignoring the contribution of ρ, because its difference is smaller than that of q_v or v. The difference in the water vapor flux between the PRE cases and the non-typhoon cases can be expressed by linear decomposition as follows (1).

$$
\begin{aligned}
\Delta(\boldsymbol{qv}) &= (\boldsymbol{qv})_{\boldsymbol{PRE}} - (\boldsymbol{qv})_{\boldsymbol{NT}} \\
&= (\boldsymbol{q}_{\boldsymbol{NT}} + \Delta\boldsymbol{q})(\boldsymbol{v}_{\boldsymbol{NT}} + \Delta\boldsymbol{v}) - (\boldsymbol{qv})_{\boldsymbol{NT}} \\
&= \boldsymbol{q}_{\boldsymbol{NT}} \cdot \Delta\boldsymbol{v} + \Delta\boldsymbol{q} \cdot \boldsymbol{v}_{\boldsymbol{NT}} + \Delta\boldsymbol{q} \cdot \Delta\boldsymbol{v} + \boldsymbol{q}_{\boldsymbol{NT}} \cdot \boldsymbol{v}_{\boldsymbol{NT}} - (\boldsymbol{qv})_{\boldsymbol{NT}} \qquad (1)
\end{aligned}
$$

Here, the values with subscripts *PRE* and *NT* represent the PRE and non-typhoon cases, respectively, and Δ represents the difference between the two cases [$\Delta(\,) = (\,)_{PRE} - (\,)_{NT}$]. The first term $\boldsymbol{q}_{\boldsymbol{NT}} \cdot \Delta\boldsymbol{v}$ of equation (1) represents the contribution from the anomaly in the wind speed, the second term $\Delta\boldsymbol{q} \cdot \boldsymbol{v}_{\boldsymbol{NT}}$ represents the contribution from the anomaly in the water vapor mixing ratio. The value of the fourth term $\boldsymbol{q}_{\boldsymbol{NT}} \cdot \boldsymbol{v}_{\boldsymbol{NT}}$ minus the fifth term $(\boldsymbol{qv})_{\boldsymbol{NT}}$ is smaller than the third term $\Delta\boldsymbol{q} \cdot \Delta\boldsymbol{v}$. The results up to the third term in equation (1) are shown in Fig. 13. The contribution from the anomaly in wind speed (Fig. 13a) was the largest; that is, the contribution of the wind speed to the difference in the northward water vapor flux component was larger than that of the water vapor mixing ratio. The difference in the water vapor flux between the PRE cases and the non-typhoon cases can be approximated by the first term of equation (1) [$\Delta(\boldsymbol{qv}) \cong \boldsymbol{q_{NT}} \cdot \Delta\boldsymbol{v}$]. It is interesting that the effect of the water vapor flux is also observed above the middle troposphere in the PRE cases. The cause of the enhanced water vapor flux in the middle troposphere is a topic for future studies.

5. Conclusions

The purpose of this study is to clarify the statistical characteristics of precipitation in Japan associated with PRE, i.e., remote precipitation indirectly caused by typhoons, in September for 40 years from 1980 to 2019. In particular, we examined the locations, the tracks, and the intensity of the typhoons that cause PRE in Japan. In addition, we studied the differences in the environmental fields between three cases: the cases of PRE (PRE cases), the cases in which remote precipitation did not occur (non-PRE cases), and the cases in which heavy precipitation in Japan was not affected by typhoons (non-typhoon cases).

Statistical analysis of the PRE cases showed that PRE tended to occur when the typhoons were located over the southern or southwestern oceans of mainland Japan and were moving northward or recurving. The distance between the typhoons and the precipitation areas of PRE exceeded 1000 km in most cases. PRE occurred regardless of typhoon intensity; in some cases, PRE occurred when the central pressure of the typhoons was above 980 hPa. We also found that most of the PRE occurred in the weakening phase of the typhoons. No characteristic relationship was found between the central pressure of the typhoons and the maximum daily precipitation at the time of PRE occurrence.

The results of the composite analysis of the three cases showed the following characteristics. First, the extension of the subtropical high south of Japan was retreating for the PRE cases during the two days before PRE occurrence, while it was strengthening for the non-PRE cases. Second, the 200 hPa jet streak entrance was close to the precipitation area for the PRE cases; specifically, the precipitation occurred on the equatorward jet streak entrance. By contrast, for the non-PRE cases, the 200 hPa jet streak entrance was located to the west compared to the PRE cases, and thus heavy precipitation was not enhanced around Japan. Third, the 850 hPa equivalent potential temperature showed that the precipitation area was characterized by the frontal zone for the PRE cases. Fourth, the vertical cross-section of the northward water vapor flux component showed that the water vapor was transported to Japan in the PRE cases and the non-typhoon cases. In both cases, water vapor transport from the lower troposphere was prominent; in the PRE cases, water vapor transport from the middle troposphere was also observed. In addition, the contribution of the wind speed to this difference in the water vapor flux was greater than that of the water vapor mixing ratio.

We have shown in this study that various factors were involved in PRE occurrence in Japan. Although several characteristics were consistent with previous PRE studies, there are still factors that are not yet clear. The mechanism of interaction between typhoons and the subtropical high and the extent to which water vapor around typhoons contributes to PRE will require further investigation. Based on the results obtained in this study, it is hoped that the mechanisms of PRE occurrence and strengthening in Japan will be clarified.

Declaration

The authors have no conflicts of interest to declare.

Author contributions

S.K. and **M.S.** designed this study. **S.K.** executed this study and wrote the manuscript. **S.K.** and **M.S.** edited and approved the manuscript.

Acknowledgments

This work was supported by MEXT (JPMXP1020200305) under the "Program for Promoting Researches on the Supercomputer Fugaku" (Large Ensemble Atmospheric and Environmental Prediction for Disaster Prevention and Mitigation) and Grant-in-Aid for Scientific Research (C) (21K03657) from Japan Society for the Promotion of Science (JSPS). The Best Track Data (https://www.jma.go.jp/jma/jma-eng/jma-center/rsmc-hp-pub-eg/besttrack.html) was provided by RSMC Tokyo-Typhoon Center. The ERA5 data (Climate data store: https://cds.climate.copernicus.eu/cdsapp#!/search?text=ERA5&type=dataset) was provided by ECMWF. The GSMaP data (https://sharaku.eorc.jaxa.

jp/GSMaP/index_j.htm) was provided by Japan Aerospace Exploration Agency (JAXA).

References

Bosart, L. F., and F. H. Carr, 1978: A case study of excessive rainfall centered around Wellsville, New York, 20–21 June 1972. *Mon. Wea. Rev.*, **106**, 348–362.

Bosart, L. F., J. M. Cordeira, T. J. Galarneau Jr., B. J. Moore, and H. M. Archambault, 2012: An analysis of multiple predecessor rain events ahead of Tropical Cyclones Ike and Lowell: 10–15 September 2008. *Mon. Wea. Rev.*, **140**, 1081–1107.

Byun, K. Y., and T. Y. Lee, 2012: Remote effects of tropical cyclones on heavy rainfall over the Korean peninsula–statistical and composite analysis. *Tellus A*, **64**, 14983.

Cote, M. R., 2007: Predecessor rain events in advance of tropical cyclones. M.S. thesis, Dept. of Atmospheric and Environmental Sciences, University at Albany, State University of New York, 200 pp.

Galarneau, T. J. Jr., L. F. Bosart, and R. S. Schumacher, 2010: Predecessor rain events ahead of tropical cyclones. *Mon. Wea. Rev.*, **138**, 3272–3297.

Hersbach, H., B. Bell, P. Berrisford, G. Biavati, A. Horányi, J. Muñoz Sabater, J. Nicolas, C. Peubey, R. Radu, I. Rozum, D. Schepers, A. Simmons, C. Soci, D. Dee, J-N. Thépaut, 2018a: ERA5 hourly data on pressure levels from 1979 to present. Copernicus Climate Change Service (C3S) Climate Data Store (CDS). Accessed on 16 September 2020, 10.24381/cds.bd0915c6.

—— 2018b: ERA5 hourly data on single levels from 1979 to present. Copernicus Climate Change Service (C3S) Climate Data Store (CDS). Accessed on 17 July 2020, 10.24381/cds.adbb2d47.

—— 2019: ERA5 monthly averaged data on single levels from 1979 to present. Copernicus Climate Change Service (C3S) Climate Data Store (CDS). Accessed on 4 December 2020, 10.24381/cds.f17050d7.

Hirata, H., and R. Kawamura, 2014: Scale interaction between typhoons and the North Pacific subtropical high and associated remote effects during the Baiu/Meiyu season. *J. Geophys. Res.: Atmos.*, **119**, 5157–5170.

Kawamura, R., and T. Ogasawara, 2006: On the role of typhoons in generating PJ teleconnection patterns over the western North Pacific in late summer. *SOLA*, **2**, 37–40.

Kitabatake, N., 2002: The role of convective instability and frontogenetic circulation in the torrential rainfall in the Tokai District on 11-12 September 2000. *Pap. Meteor. Geophys.*, **53**, 91–108. (in Japanese)

Kitabatake, N., 2012: PRE (Predecessor Rain Event). *Tenki*, **59**, 171−172. (in Japanese)

Kubota, T., S. Shige, H. Hashizume, K. Aonashi, N. Takahashi, S. Seto, M. Hirose, Y. N. Takayabu, K. Nakagawa, K. Iwanami, T. Ushio, M. Kachi, and K. Okamoto, 2007: Global Precipitation Map using Satellite-borne Microwave Radiometers by the GSMaP Project: Production and Validation. *IEEE Trans. Geosci. Remote Sens.*, **45**, 2259-2275.

Moore, B. J., L. F. Bosart, D. Keyser, and M. L. Jurewicz, 2013: Synoptic-scale environments of predecessor rain events occurring east of the Rocky Mountains in association with Atlantic basin tropical cyclones. *Mon. Wea. Rev.*, **141**, 1022–1047.

Murata, A., 2009: A mechanism for heavy precipitation over the Kii Peninsula accompanying Typhoon Meari (2004). *J. Meteor. Soc. Japan.*, **87**, 101–117.

Ninomiya, K., 2013: Influence of a distantly located typhoon, a weak westerly trough and orography on the intense rainfall on 14-15 September 1965 over Gifu and Fukui prefecture of Japan. *J. Meteor. Soc. Japan.*, **91**, 489–506.

Ross, R. J., and Y. Kurihara, 1995: A numerical study on influences of Hurricane Gloria (1985) on the environment. *Mon. Wea. Rev.,* **123**, 332–346.

Saito, K., 2019: On the northward ageostrophic winds associated with a tropical cyclone. *SOLA*, **15**, 222–227.

Saito, K., and T. Matsunobu, 2020: Northward ageostrophic winds associated with a tropical cyclone. Part 2: Moisture transport and its impact on PRE. *SOLA*, **16**, 198–205.

Schumacher, R. S., and T. J. Galarneau Jr., 2012: Moisture transport into midlatitudes ahead of recurving tropical cyclones and its relevance in two predecessor rain events. *Mon. Wea. Rev.*, **140**, 1810–1827.

Schumacher, R. S., T. J. Galarneau Jr., and L. F. Bosart, 2011: Distant effects of a recurving tropical cyclone on rainfall in a midlatitude convective system: A high-impact predecessor rain event. *Mon. Wea. Rev.*, **139**, 650–667.

Tsuguti, H., and T. Kato, 2014: Objective extraction of heavy rainfall events and statistical analysis on their characteristic features. *Tenki*, **61**, 455–469. (in Japanese)

Wang, Y., Y. Wang, and H. Fudeyasu, 2009: The role of Typhoon Songda (2004) in producing distantly located heavy rainfall in Japan. *Mon. Wea. Rev.*, **137**, 3699–3716.

Yamada, K., and R. Kawamura, 2007: Dynamical link between typhoon activity and the PJ teleconnection pattern from early summer to autumn as revealed by the JRA-25 reanalysis. *SOLA*, **3**, 65–68.

Yoshida, K., and H. Itoh, 2012: Indirect effects of tropical cyclones on heavy rainfall events in Kyushu, Japan, during the Baiu season. *J. Meteor. Soc. Japan.*, **90**, 377–401.

Yuan, J., D. Zhao, R. Yang, and H. Yang, 2018: Predecessor rain events over China's low-latitude highlands associated with Bay of Bengal tropical cyclones. *Climate Dyn.*, **50**, 825–843.

List of Figures

Fig. 1. (a) Locations of typhoon centers in the 58 PRE cases (blue dots). **(b)** Locations of precipitation centers in the 58 PRE cases (blue dots). **(c)** Same as in (a) but for the 31 non-PRE cases (blue dots). **(d)** Same as in (b) but for the 24 non-typhoon cases (blue dots). The red rectangle shows the extraction area [130–150°E, 30–40°N].

Fig. 2. (a–d) Tracks of typhoons in the PRE cases, divided into 10-year periods: 1980–1989, 1990–1999, 2000–2009 and 2010–2019. The blue dots show the typhoon centers. **(e–h)** Same as in (a–d) but for the non-PRE cases. The blue dots show the typhoon

centers. The red rectangle shows the extraction area [130–150°E, 30–40°N].

Fig. 3. **(a)** Histogram of the distance (km) between typhoon centers and precipitation centers in the PRE cases. **(b)** Histogram of the direction of precipitation centers from typhoon centers in the PRE cases (azimuth; °), excluding four cases. **(c)** Histogram of the central pressures (hPa) of typhoons in the PRE cases. **(d)** Same as in (c) but for the non-PRE cases.

Fig. 4. Histogram of typhoon central pressure (hPa) and maximum daily precipitation (mm) in the PRE cases, excluding one case.

Fig. 5. Composite of 500 hPa geopotential height (contour; m), precipitable water (shaded; mm) and vertical integrals of water vapor flux (vector; kg m^{-1} s^{-1}) for the 58 PRE cases on **(a)** Day–2, **(b)** Day–1, **(c)** Day0, and **(d)** Day+1. The contour interval is 60 m. The reference arrow is 400 kg m^{-1} s^{-1}. The red rectangle shows the extraction area [130–150°E, 30–40°N]. The green cross mark shows the median point of precipitation on Day0. The red dots on Day0 show the locations of typhoon centers relative to the median point of precipitation.

Fig. 6. Composite of 200 hPa geopotential height (black contour; dam), 200 hPa isotach (blue contour; m s^{-1}), 700 hPa vertical velocity (shaded; Pa s^{-1}) and 850 hPa horizontal wind (vector; m s^{-1}) for the 58 PRE cases on **(a)** Day–2, **(b)** Day–1, **(c)** Day0, and **(d)** Day+1. The black contour interval is 10 dam and the blue contour interval is 5 m s^{-1} (35, 40, 45 m s^{-1}). The reference arrow is 10 m s^{-1}. The red rectangle

shows the extraction area [130–150°E, 30–40°N]. The green cross mark shows the median point of precipitation on Day0. The blue dots on Day0 show the locations of typhoon centers relative to the median point of precipitation.

Fig. 7. **(a)** Composite of 850 hPa equivalent potential temperature (shaded and contour; K) for the 58 PRE cases on Day0. The contour interval is 3 K. The black rectangle shows the extraction area [130–150°E, 30–40°N]. The green cross mark shows the median point of precipitation. **(b)** Composite of vertical northward water vapor flux (shaded; g m^{-2} s^{-1}) for the 58 PRE cases on Day0 between 130°E and 150°E along the latitude 30°N.

Fig. 8. Composite of 500 hPa geopotential height (contour; m), precipitable water (shaded; mm) and vertical integrals of water vapor flux (vector; kg m^{-1} s^{-1}) for 16 non-PRE cases on **(a)** Day–2, **(b)** Day–1, **(c)** Day0, and **(d)** Day+1. The contour interval is 60 m. The reference arrow is 400 kg m^{-1} s^{-1}. The red rectangle shows the extraction area [130–150°E, 30–40°N]. The red dots on Day0 show the locations of typhoon centers.

Fig. 9. Composite of 200 hPa geopotential height (black contour; dam), 200 hPa isotach (blue contour; m s^{-1}), 700 hPa vertical velocity (shaded; Pa s^{-1}) and 850 hPa horizontal wind (vector; m s^{-1}) for 16 non-PRE cases on **(a)** Day–2, **(b)** Day–1, **(c)** Day0, and **(d)** Day+1. The black contour interval is 10 dam and the blue contour interval is 5 m s^{-1} (35, 40, 45 m s^{-1}). The reference arrow is 10 m s^{-1}. The red rectangle shows the extraction area [130–150°E, 30–40°N]. The blue dots on Day0 show the

locations of typhoon centers.

Fig. 10. Composite of 850 hPa equivalent potential temperature (shaded and contour; K) for 16 non-PRE cases on Day0. The contour interval is 3 K. The black rectangle shows the extraction area [130–150°E, 30–40°N].

Fig. 11. **(a)** Composite of 500 hPa geopotential height (contour; m), precipitable water (shaded; mm) and vertical integral of water vapor flux (vector; kg m^{-1} s^{-1}) for the 24 non-typhoon cases on Day0. The contour interval is 60 m. The reference arrow is 400 kg m^{-1} s^{-1}. The red rectangle shows the extraction area [130–150°E, 30–40°N]. The green cross mark shows the median point of precipitation. **(b)** Same as in (a) but for 200 hPa geopotential height (black contour; dam), 200 hPa isotach (blue contour; m s^{-1}), 700 hPa vertical velocity (shaded; Pa s^{-1}) and 850 hPa horizontal wind (vector; m s^{-1}) on Day0. The black contour interval is 10 dam and the blue contour interval is 5 m s^{-1} (35, 40, 45 m s^{-1}). The reference arrow is 10 m s^{-1}. **(c)** Same as in (a) but for 850 hPa equivalent potential temperature on Day0 (shaded and contour; K). The contour interval is 3 K. The black rectangle shows the extraction area [130–150°E, 30–40°N]. **(d)** Same as in (a) but for vertical northward water vapor flux (shaded; g m^{-2} s^{-1}) on Day0 between 130°E and 150°E along the latitude 30°N.

Fig. 12. Time series of composite for 500 hPa geopotential height (m) from Day–2 to Day0 (18 PRE cases, red; 16 non-PRE cases, blue). The 500 hPa geopotential height is

averaged over the region [130–140°E, 27.5–32.5°N], and the value 48 hours before PRE occurrence is set to 0 m. The whisker marks represent standard deviation.

Fig. 13. Each component of the linear decomposition of vertical northward water vapor flux (not including air density ρ) on Day0 between 130°E and 150°E along the latitude 30°N (shaded; g kg^{-1} * m s^{-1}). **(a)** $\boldsymbol{q_{NT}} \cdot \Delta \boldsymbol{v}$, **(b)** $\Delta \boldsymbol{q} \cdot \boldsymbol{v_{NT}}$, **(c)** $\Delta \boldsymbol{q} \cdot \Delta \boldsymbol{v}$.

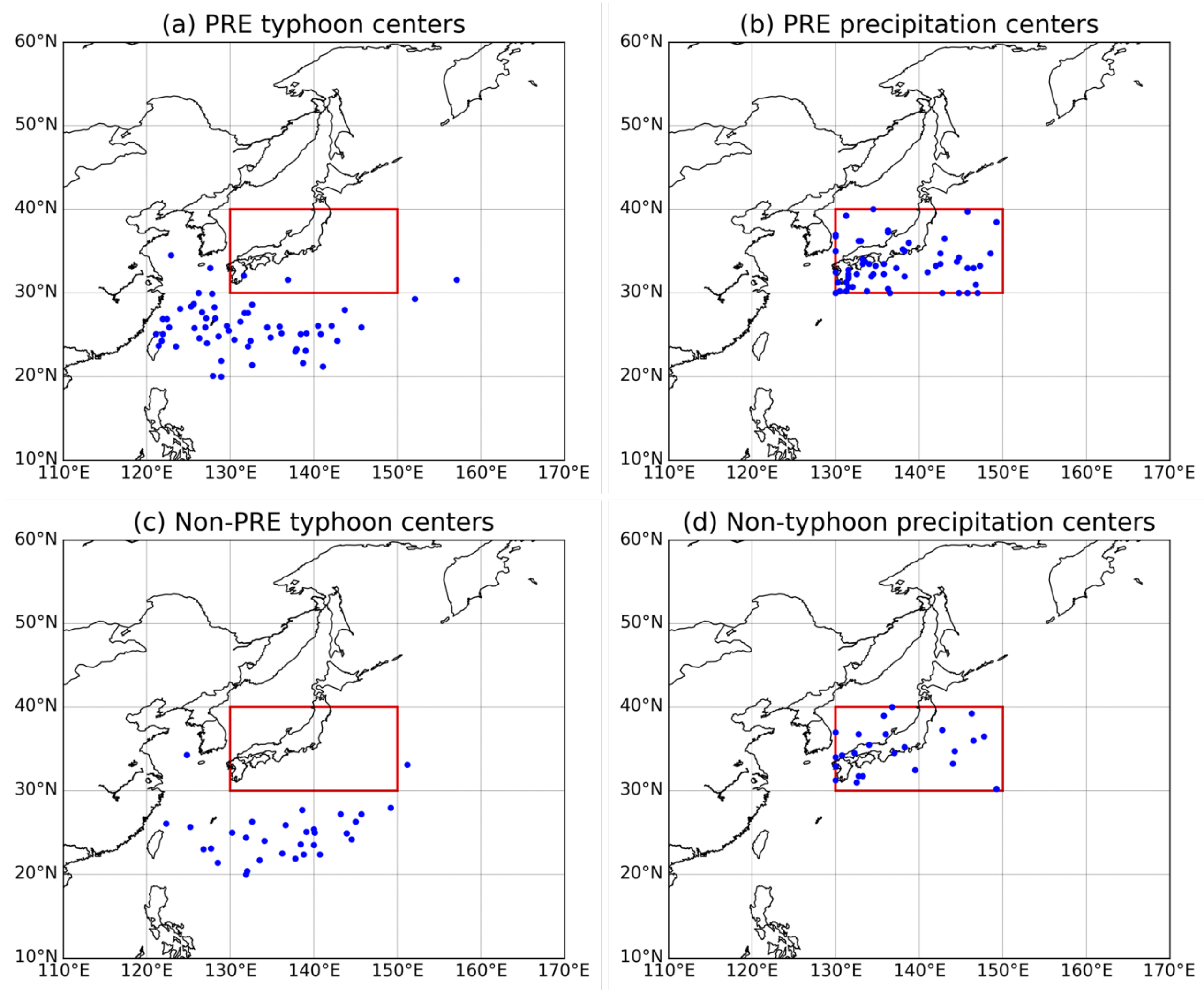

Fig. 1. (a) Locations of typhoon centers in the 58 PRE cases (blue dots). **(b)** Locations of precipitation centers in the 58 PRE cases (blue dots). **(c)** Same as in (a) but for the 31 non-PRE cases (blue dots). **(d)** Same as in (b) but for the 24 non-typhoon cases (blue dots). The red rectangle shows the extraction area [130–150°E, 30–40°N].

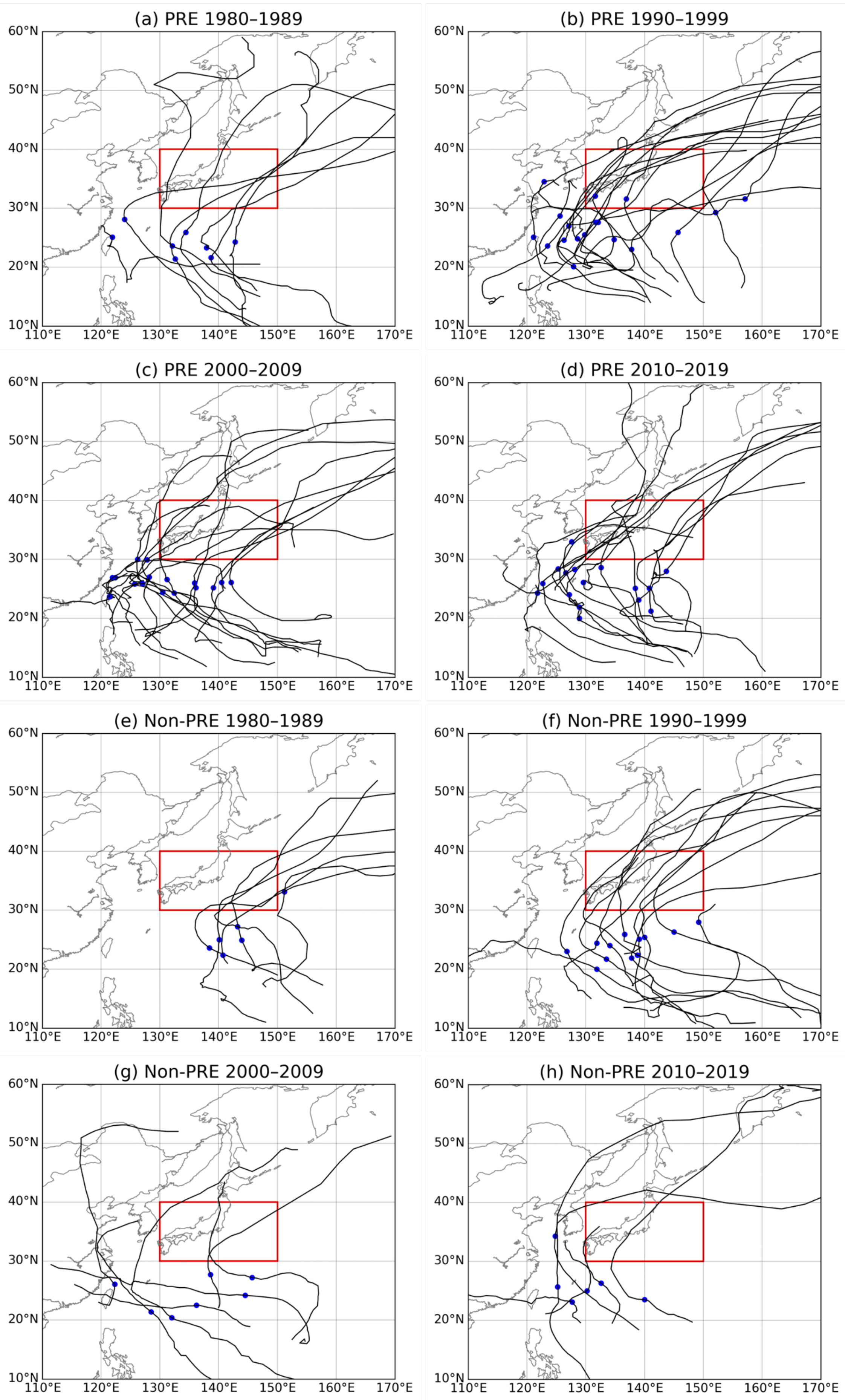
(a) PRE 1980–1989
(b) PRE 1990–1999
(c) PRE 2000–2009
(d) PRE 2010–2019
(e) Non-PRE 1980–1989
(f) Non-PRE 1990–1999
(g) Non-PRE 2000–2009
(h) Non-PRE 2010–2019
60°N
50°N
40°N
30°N
20°N
10°N
110°E
120°E
130°E
140°E
150°E
160°E
170°E

Fig. 2. (a–d) Tracks of typhoons in the PRE cases, divided into 10-year periods: 1980–1989, 1990–1999, 2000–2009 and 2010–2019. The blue dots show the typhoon centers. **(e–h)** Same as in (a–d) but for the non-PRE cases. The blue dots show the typhoon centers. The red rectangle shows the extraction area [130–150°E, 30–40°N].

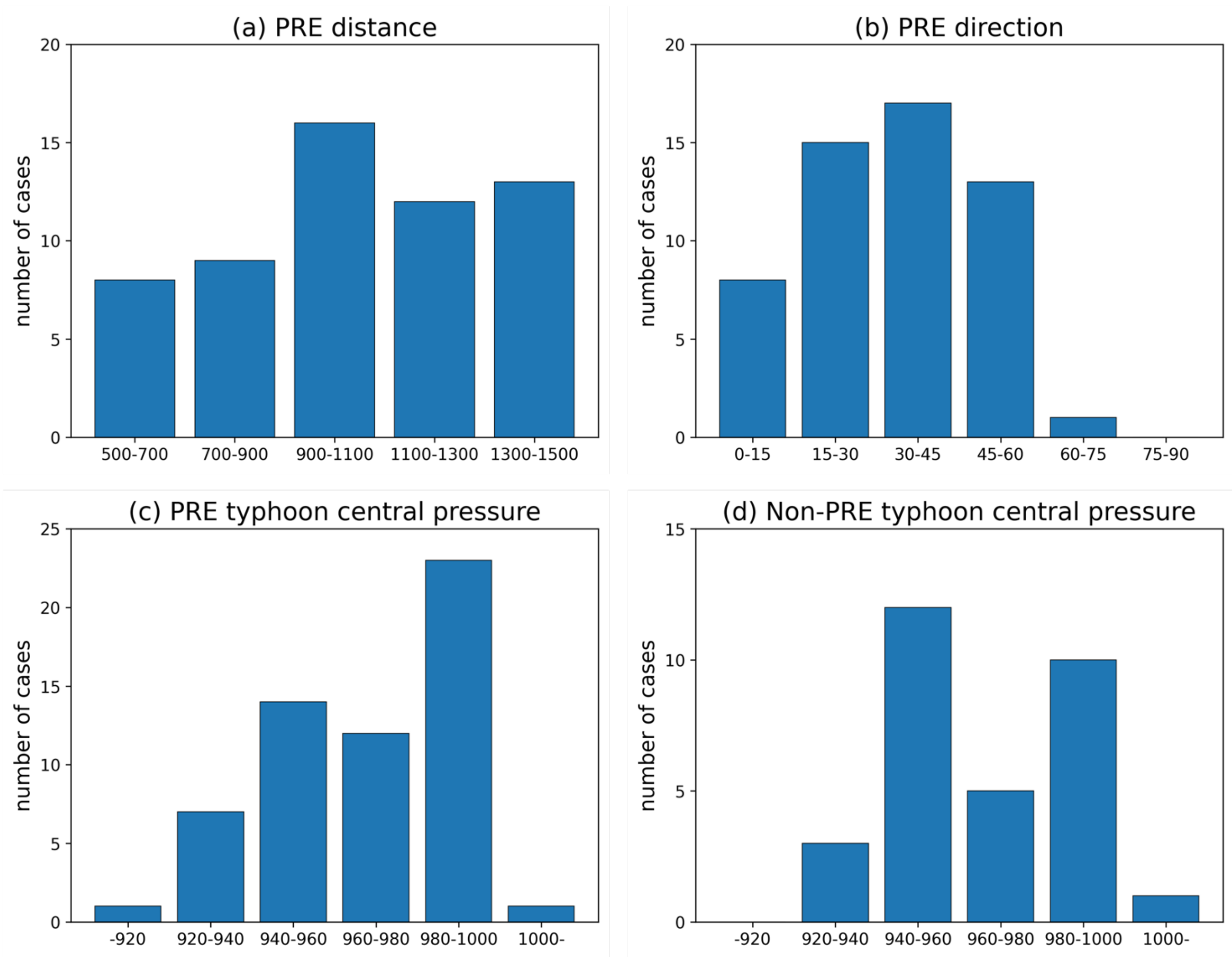

Fig. 3. (a) Histogram of the distance (km) between typhoon centers and precipitation centers in the PRE cases. **(b)** Histogram of the direction of precipitation centers from typhoon

centers in the PRE cases (azimuth; °), excluding four cases. **(c)** Histogram of the central pressures (hPa) of typhoons in the PRE cases. **(d)** Same as in (c) but for the non-PRE cases.

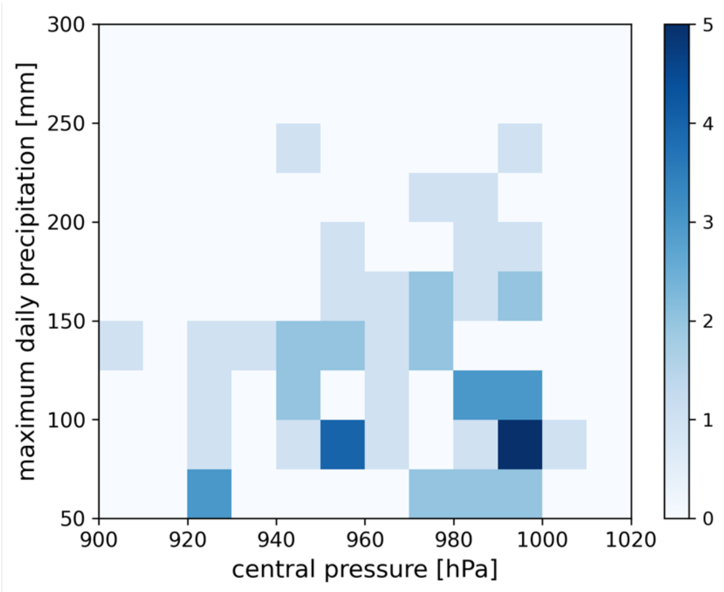

Fig. 4. Histogram of typhoon central pressure (hPa) and maximum daily precipitation (mm) in the PRE cases, excluding one case.

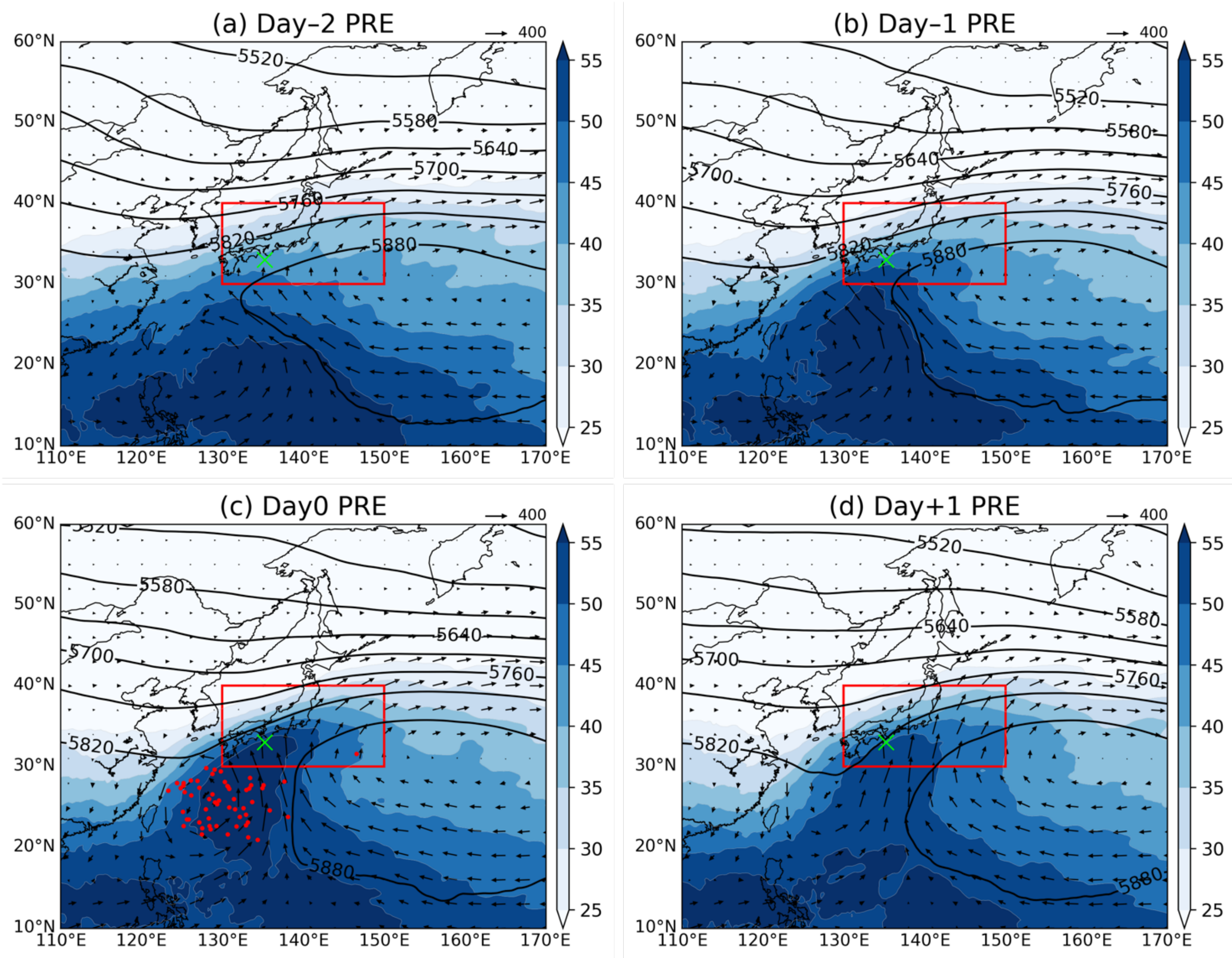

Fig. 5. Composite of 500 hPa geopotential height (contour; m), precipitable water (shaded; mm) and vertical integrals of water vapor flux (vector; kg m^{-1} s^{-1}) for the 58 PRE cases on **(a)** Day–2, **(b)** Day–1, **(c)** Day0, and **(d)** Day+1. The contour interval is 60 m. The reference arrow is 400 kg m^{-1} s^{-1}. The red rectangle shows the extraction area [130–150°E, 30–40°N]. The green cross mark shows the median point of precipitation on Day0. The red dots on Day0 show the locations of typhoon centers relative to the median point of precipitation.

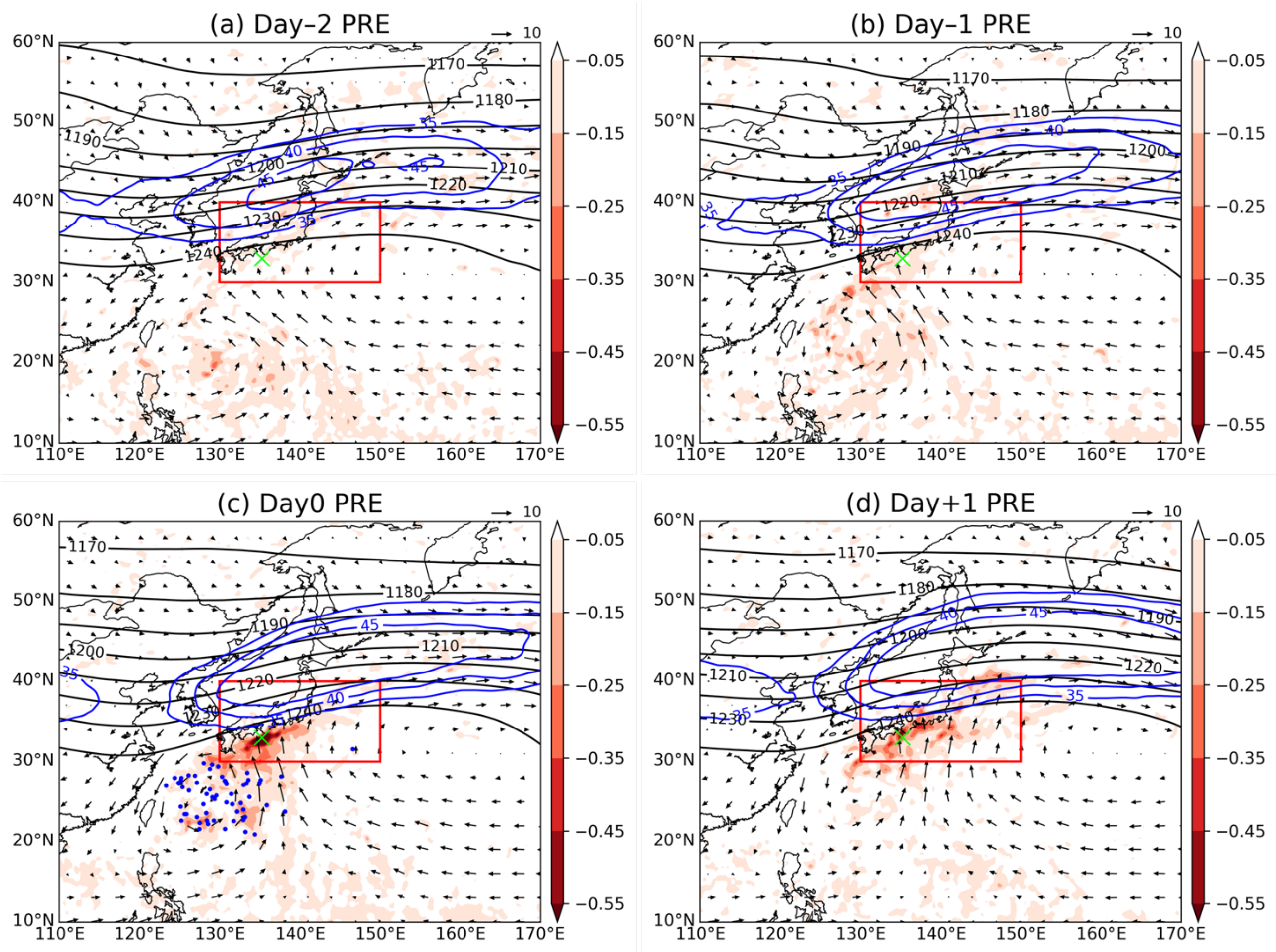

Fig. 6. Composite of 200 hPa geopotential height (black contour; dam), 200 hPa isotach (blue contour; m s^{-1}), 700 hPa vertical velocity (shaded; Pa s^{-1}) and 850 hPa horizontal wind (vector; m s^{-1}) for the 58 PRE cases on **(a)** Day–2, **(b)** Day–1, **(c)** Day0, and **(d)** Day+1. The black contour interval is 10 dam and the blue contour interval is 5 m s^{-1} (35, 40, 45 m s^{-1}). The reference arrow is 10 m s^{-1}. The red rectangle shows the extraction area [130–150°E, 30–40°N]. The green cross mark shows the median point of precipitation on Day0. The blue dots on Day0 show the locations of typhoon centers relative to the median point of precipitation.

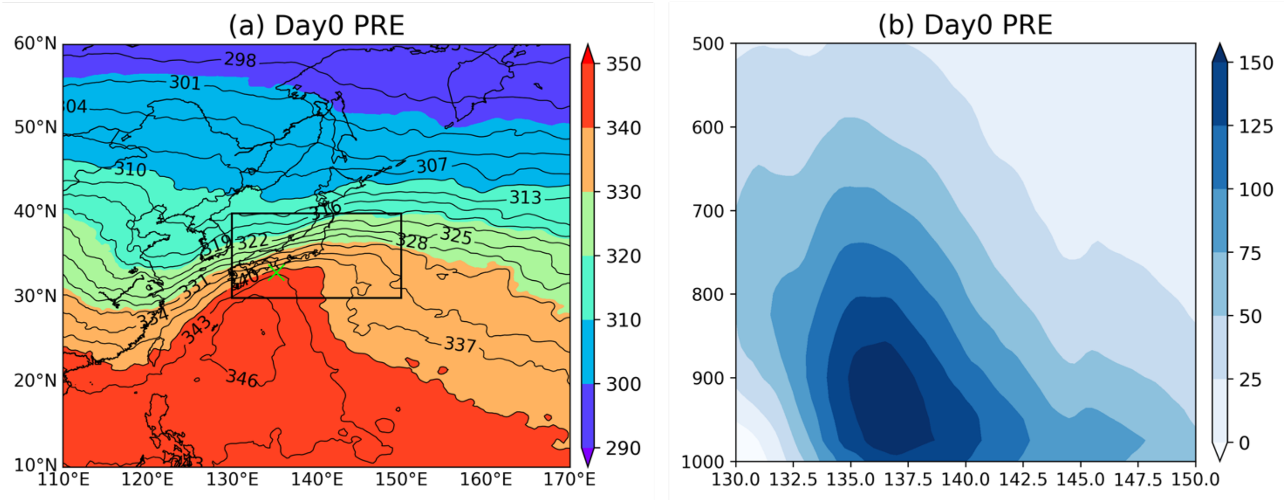

Fig. 7. (a) Composite of 850 hPa equivalent potential temperature (shaded and contour; K) for the 58 PRE cases on Day0. The contour interval is 3 K. The black rectangle shows the extraction area [130–150°E, 30–40°N]. The green cross mark shows the median point of precipitation. **(b)** Composite of vertical northward water vapor flux (shaded; g m^{-2} s^{-1}) for the 58 PRE cases on Day0 between 130°E and 150°E along the latitude 30°N.

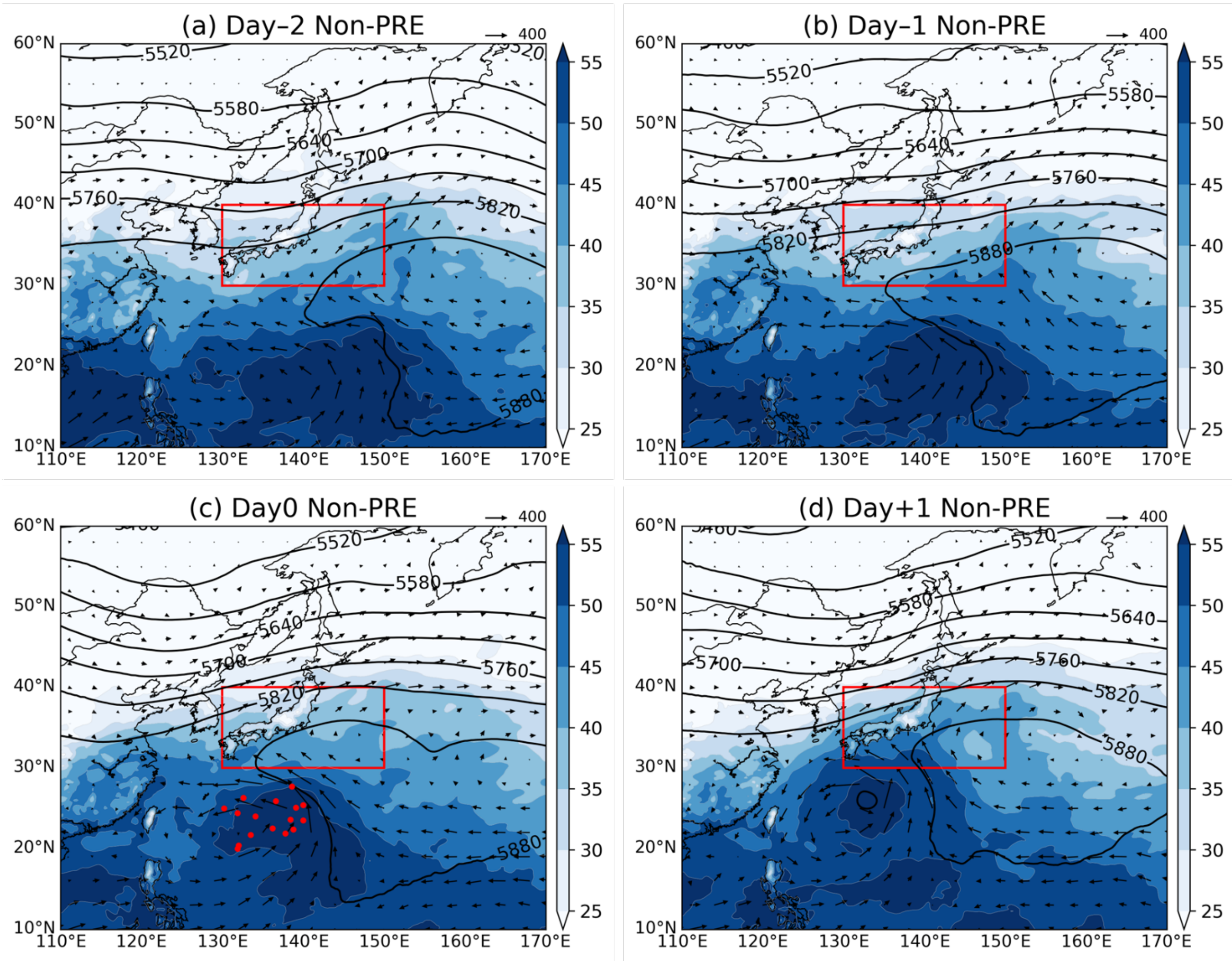

Fig. 8. Composite of 500 hPa geopotential height (contour; m), precipitable water (shaded; mm) and vertical integrals of water vapor flux (vector; kg m^{-1} s^{-1}) for 16 non-PRE cases on **(a)** Day–2, **(b)** Day–1, **(c)** Day0, and **(d)** Day+1. The contour interval is 60 m. The reference arrow is 400 kg m^{-1} s^{-1}. The red rectangle shows the extraction area [130–150°E, 30–40°N]. The red dots on Day0 show the locations of typhoon centers.

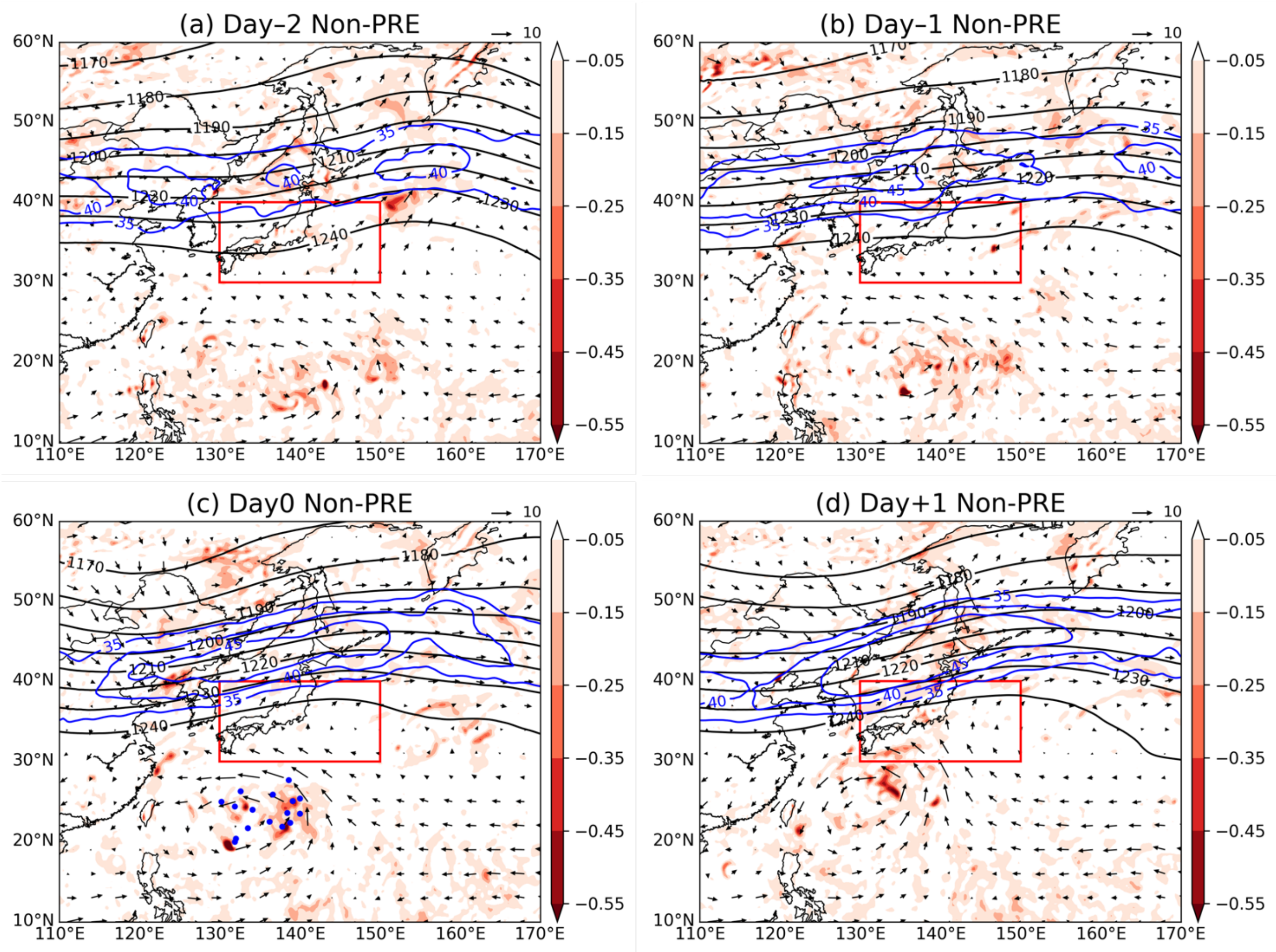

Fig. 9. Composite of 200 hPa geopotential height (black contour; dam), 200 hPa isotach (blue contour; m s^{-1}), 700 hPa vertical velocity (shaded; Pa s^{-1}) and 850 hPa horizontal wind (vector; m s^{-1}) for 16 non-PRE cases on **(a)** Day–2, **(b)** Day–1, **(c)** Day0, and **(d)** Day+1. The black contour interval is 10 dam and the blue contour interval is 5 m s^{-1} (35, 40, 45 m s^{-1}). The reference arrow is 10 m s^{-1}. The red rectangle shows the extraction area [130–150°E, 30–40°N]. The blue dots on Day0 show the locations of typhoon centers.

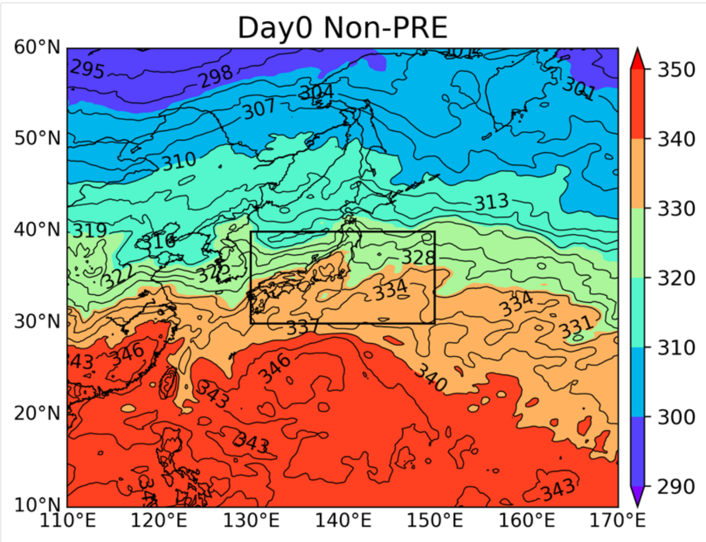

Fig. 10. Composite of 850 hPa equivalent potential temperature (shaded and contour; K) for 16 non-PRE cases on Day0. The contour interval is 3 K. The black rectangle shows the extraction area [130–150°E, 30–40°N].

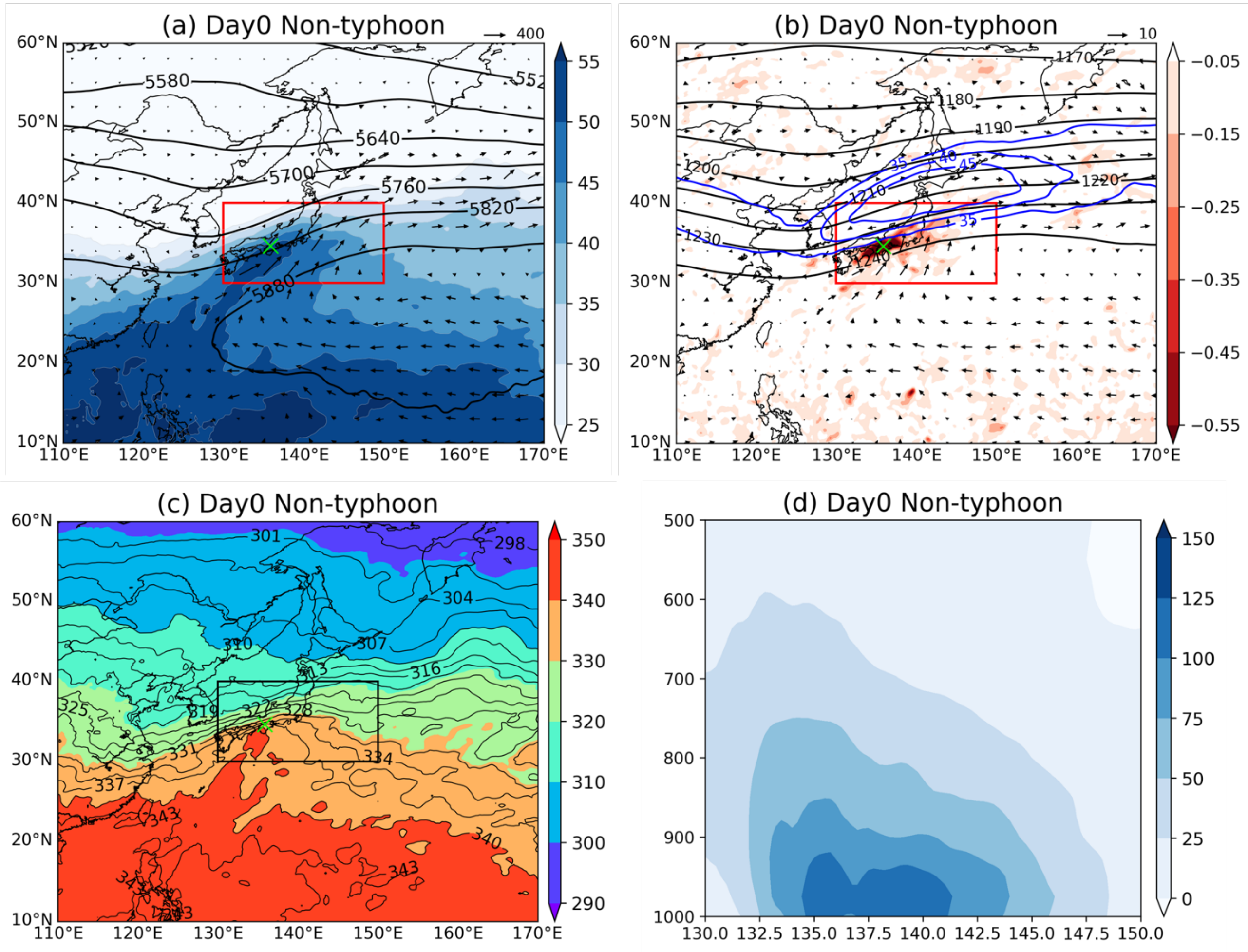

Fig. 11. (a) Composite of 500 hPa geopotential height (contour; m), precipitable water (shaded; mm) and vertical integral of water vapor flux (vector; kg m^{-1} s^{-1}) for the 24 non-typhoon cases on Day0. The contour interval is 60 m. The reference arrow is 400 kg m^{-1} s^{-1}. The red rectangle shows the extraction area [130–150°E, 30–40°N]. The green cross mark shows the median point of precipitation. **(b)** Same as in (a) but for 200 hPa geopotential height (black contour; dam), 200 hPa isotach (blue contour; m s^{-1}), 700 hPa vertical velocity (shaded; Pa s^{-1}) and 850 hPa horizontal wind (vector; m s^{-1}) on Day0. The black contour interval is 10 dam and the blue contour interval is 5 m s^{-1} (35, 40, 45

m s^{-1}). The reference arrow is 10 m s^{-1}. **(c)** Same as in (a) but for 850 hPa equivalent potential temperature on Day0 (shaded and contour; K). The contour interval is 3 K. The black rectangle shows the extraction area [130–150°E, 30–40°N]. **(d)** Same as in (a) but for vertical northward water vapor flux (shaded; g m^{-2} s^{-1}) on Day0 between 130°E and 150°E along the latitude 30°N.

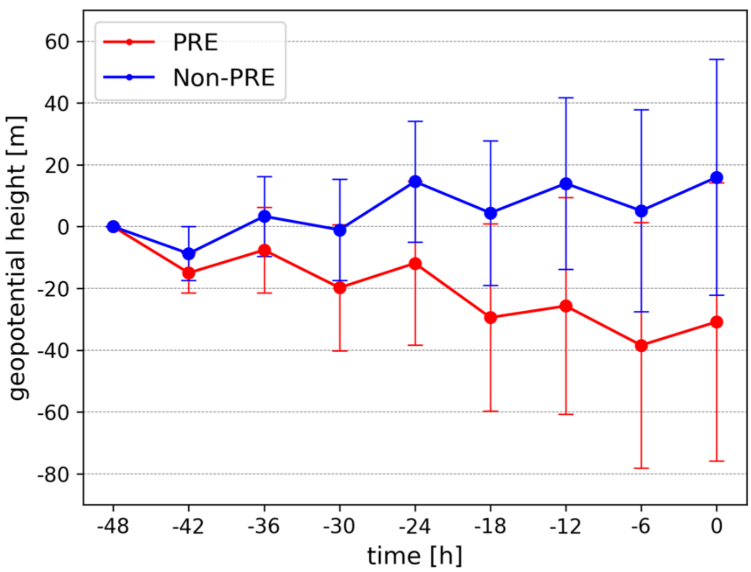

Fig. 12. Time series of composite for 500 hPa geopotential height (m) from Day–2 to Day0 (18 PRE cases, red; 16 non-PRE cases, blue). The 500 hPa geopotential height is averaged over the region [130–140°E, 27.5–32.5°N], and the value 48 hours before PRE occurrence is set to 0 m. The whisker marks represent standard deviation.

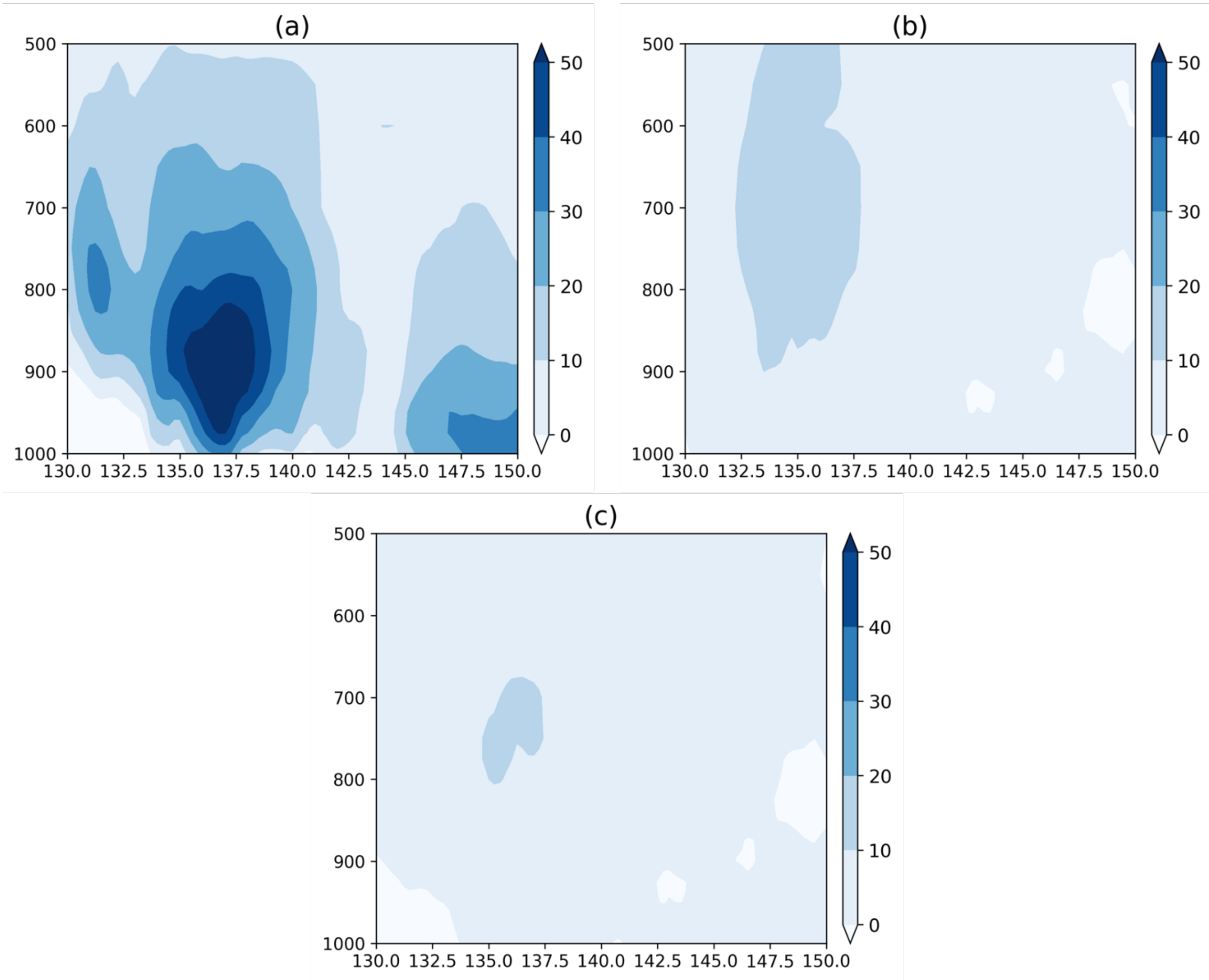

Fig. 13. Each component of the linear decomposition of vertical northward water vapor flux (not including air density ρ) on Day0 between 130°E and 150°E along the latitude 30°N (shaded; g kg^{-1} * m s^{-1}). **(a)** $\boldsymbol{q_{NT}} \cdot \Delta \boldsymbol{v}$, **(b)** $\Delta \boldsymbol{q} \cdot \boldsymbol{v_{NT}}$, **(c)** $\Delta \boldsymbol{q} \cdot \Delta \boldsymbol{v}$.